

Understanding the differences between microporous and mesoporous synthesis through the phase behavior of silica

Joseph M. Fedeyko, Dionisios G. Vlachos *, Raul F. Lobo *

Center for Catalytic Science and Technology, Department of Chemical Engineering, University of Delaware, Newark, DE 19716, USA

Accepted 28 October 2005

Available online 4 January 2006

Dedicated to the late Denise Barthomeuf, George Kokotailo and Sergey P. Zhdanov in appreciation of their outstanding contributions to zeolite science

Abstract

The link between M41S mesoporous silicates and all-silica zeolites during the initial stages of synthesis is analyzed with small-angle scattering and conductivity experiments. The phase behavior of silica in aqueous solutions is studied for a family of quaternary ammonium hydroxides, from tetramethylammonium to dodecyltrimethylammonium. All solutions exhibit a critical aggregation concentration at a 1:1 $\text{SiO}_2:[\text{OH}^-]_{\text{initial}}$ molar ratio with solutions containing short chain compounds forming optically transparent (clear) nanoparticle suspensions, and solutions of long chain compounds phase separating into a solid and a liquid phase. The solid phase is analyzed with X-ray diffraction and thermogravimetric analysis and is found to have a hexagonal structure similar to MCM-41. Mid-sized chain length compounds form solutions containing both the phase separated solid and nanoparticles. In addition to studying phase behavior, the role of attractive hydrophobic interactions is studied using water/ethanol solutions. In ethanolic solutions, the entire family of quaternary ammonium compounds are found to form stable nanoparticle suspensions.

© 2005 Elsevier Inc. All rights reserved.

Keywords: Zeolite synthesis; Silica nanoparticles; MCM-41; Self-assembly; Mesoporous

1. Introduction

Porous materials synthesis has recently focused on the creation of functional materials tailored to specific processes through directed assembly strategies [1,2]. Two successful examples of this ongoing effort are of course zeolites and ordered mesoporous silica materials. Both involve the controlled condensation of silica either from the gel or solution phase. Industrial application of zeolites, with pores below 1 nm are extensive in separations and catalysis [3–5]. Mesoporous materials have larger pore dimensions (~2 nm) leading to applications in material templating,

biological separations, controlled drug delivery and others [6–8].

On the surface, the synthesis of these two classes of materials appears quite different. Zeolitic materials form in the presence of inorganic or organic cations that function as structure directing agents (SDAs or R^+) [9]. Upon heating, the silica self assembles to form a porous-crystalline framework with the SDA occluded within the pores. In contrast, mesoporous materials form in the presence of self-associating molecules such as cationic surfactants like cetyltrimethylammonium bromide (MCM-41) [10] and block copolymers (SBA-15) [11]. In these syntheses, the condensation of silica occurs around the self-assembled organic scaffolds and leads to a final structure with an amorphous silica framework [12].

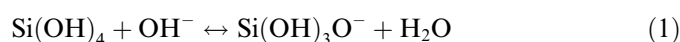
Closer examination of the two syntheses, however, reveals many similarities [13]. Both form in gel or solution phase under basic conditions ($\text{pH} \sim 10\text{--}14$). The materials

* Corresponding authors. Tel.: +1 302 831 2830; fax: +1 302 831 1048 (D.G. Vlachos); Tel.: +1 302 831 1261 (R.F. Lobo).

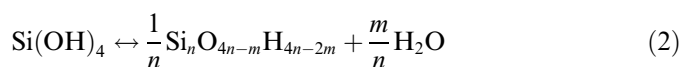
E-mail addresses: vlachos@che.udel.edu (D.G. Vlachos), lobo@che.udel.edu (R.F. Lobo).

can be prepared from most silica sources with synthesis compositions that are identical. For example, silicalite-1, an all-silica zeolite with an MFI framework-type, and MCM-41 [14] are both formed under the same synthesis conditions except for different quarternary ammonium hydroxides (molar composition, 50 ROH:9500 H₂O:83 SiO₂:332 C₂H₅OH(EtOH)). Tetrapropylammonium hydroxide (TPAOH) is used for silicalite-1; while for MCM-41, the SDA is cetyltrimethylammonium hydroxide (C₁₆tMAOH).

We recently analyzed the initial stages of silicalite-1 formation [15,16] and compared clear solutions of silica, water and tetraalkylammonium hydroxides (TAAOH). In these solutions, monomeric silica can undergo one of two reactions. First, monomeric silica can dissociate (Eq. (1)).



This reaction results in a reduction in the conductivity of the solution caused by differences in the limiting molar conductivity, λ , of OH[−] and Si(OH)₃O[−] ($\lambda_{\text{OH}^-} = 198.3 \text{ S m}^2/\text{mol}$ [17] and $\lambda_{\text{Si}(\text{OH})_3\text{O}^-} \sim 40$ [18]). Also, the reaction lowers the pH of the solution by consuming hydroxide anions. The other possible reaction is condensation, which forms silica clusters of size n (Eq. (2)).



The solution behavior is described in Fig. 1a. The initial addition of TEOS to solutions of TMAOH and H₂O causes a linear reduction of both the conductivity and hydroxide concentration, [OH[−]] with the pH decreasing from 12.6 to 10.9. Reaction 1 dominates in this region [19] leading to a solution rich in deprotonated monomeric silica species. At approximately a 1:1 molar ratio of SiO₂:[OH[−]]_{initial}, the slope of the conductivity changes abruptly. The pH in this second region is relatively constant (pH = 10.7–10.9 for 9

TMAOH: 9500 H₂O). Reaction 2 dominates in the second region where silica condensation is the main reaction. In both regions, the solutions are transparent; however beyond the critical concentration, small-angle X-ray scattering experiments show the formation of nanoparticles. We denote this concentration of initial nanoparticle formation the critical aggregation concentration (CAC), as defined for self-assembling systems [20]. A series of measurements with different initial pH from 12.0 to 13.1 were performed resulting in a silica phase diagram with monomeric and nanoparticle phases separated by a well-defined boundary (Fig. 1b). Nanoparticle formation is reversible to changes in silica or hydroxyl concentration for nanoparticles aged up to a few days that we have studied [15].

The free energy of the nanoparticles was studied as a function of size and found to have three important components: a chemical component derived from silica condensation, an electrostatic component derived from the formation of an electrical double-layer, and a surface energy component [19]. All three components were required to explain the presence of a minimum in free energy as a function of size which would be associated with the formation of a uniform set of nanoparticles. For micelle and microemulsion systems, this minimum in free energy would be dependent on the ions involved in double-layer formation leading to variations in the size or structure of the nanoparticle. However in this system, the identity of the cation does not affect nanoparticle morphology.

The phase behavior of silica in the precursor solutions can also be described in terms of the chemical potential of silica in solution, μ . As the silica concentration is increased through region I, the chemical potential of the monomer/oligomer solution, μ_1 , increases as described by [20]

$$\mu_1 = \mu_1^0 + kT \cdot \ln X_1 \quad (3)$$

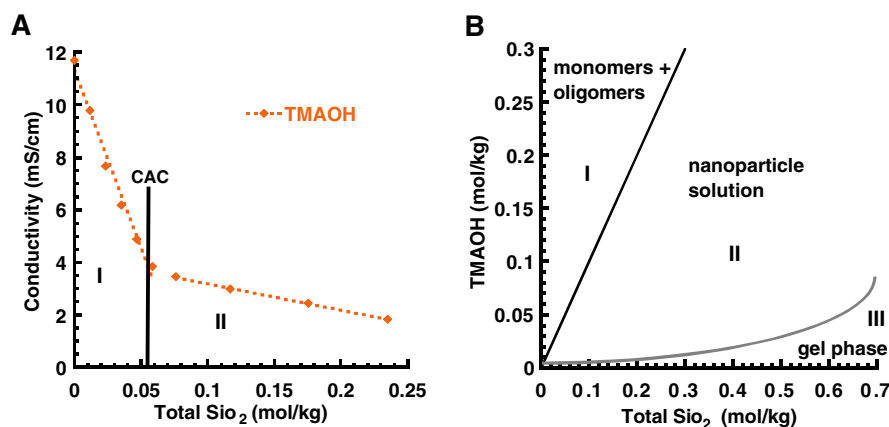


Fig. 1. Self-association of silica in TMAOH solutions. (A) The addition of silica in the form of TEOS to solutions with molar ratios of 9 TMAOH:9500 H₂O shows a drastic change in slope at a 1:1 SiO₂:[OH[−]]_{initial} molar ratio. Points are experimental data and dotted lines are linear fits to the two regions of the curve. The intersection of the two curves is defined as the critical aggregation concentration (CAC). (B) Phase behavior of silica in TMAOH solutions. A locus of CACs measured at different TMAOH concentration form a phase boundary between a phase of monomeric silica and a phase containing nanoparticles. At high silica concentrations, gels or large particles form. The line separating region II and region III suggests the position of the second boundary as it is difficult to identify with precision experimentally.

where X_1 is the silica monomer concentration, kT is the systems thermal energy and μ_1^0 is the mean interaction free energy per molecule. Eventually, μ_1 increases to a value equal to the chemical potential of the nanoparticle solution at a given concentration:

$$\mu_1 = \mu_N = \mu_N^0 + \frac{kT}{N} \cdot \ln \frac{X_N}{N} \quad (4)$$

Here N is the number of monomers in the nanoparticle and X_N is the nanoparticles concentration. This concentration results in an equilibrium between the two species. If the minimum in free energy for nanoparticle formation described above is deep enough (μ_N^0 has a steep minimum at N), this process will lead to the formation of a monodisperse set of self-assembled nanoparticles at a critical concentration [20].

In this manuscript, we investigate the aqueous chemistry of silica at compositions relevant to mesoporous silicate syntheses to determine the possible links between the formation of nanoparticles and mesoporous materials during these initial stages of material formation. The framework of silica aggregation reported in [15] will be applied to the class of MCM-41 materials originally reported by Beck et al. [10]. The resulting silica products and solutions in these syntheses are analyzed by various techniques. The phase behavior is studied under conditions where self-association of the SDA does not occur, (e.g. decyltrimethylammonium ($C_{10}tMA^+$)), and where it does, (e.g. dodecyltrimethylammonium ($C_{12}tMA^+$)). We find that the phase behavior of silica in basic solutions is independent of the self-associating nature of the SDA and that it is only the chemical potential of the silica that signals the onset of silica condensation. We conclude that silica nano-

particles and mesoporous silica materials prepared with alkylammonium cations are two different instances of the same class of physical objects.

2. Experimental


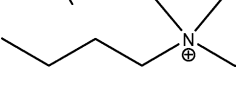
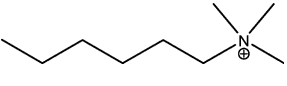
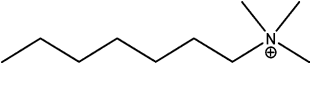
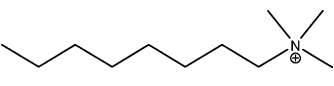
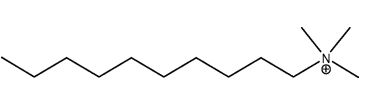
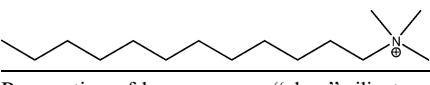
2.1. Preparation of structure directing agents

Table 1 lists the structures of the organic SDAs used in this work. Octyltrimethylammonium (C_8tMA^+), decyltrimethylammonium ($C_{10}tMA^+$), and dodecyltrimethylammonium ($C_{12}tMA^+$) bromide (Aldrich) are ion exchanged with anion exchange resin, IONAC[®] NA-38 (OH-form, Type 1, beads, J.T. Baker). Approximately 5–10 g of solid is dissolved in deionized water (~50–100 g) and fed into the column 50 ml at a time. After 1 h, the column is drained. Final solution concentrations range from 0.08 M to 0.17 M. The yield of the exchange is ~85% based on titration of the final solution with HCl.

Butyltrimethylammonium hydroxide (C_4tMAOH) is synthesized by first adding 10 g of 1-bromobutane (Aldrich) dropwise to 8.63 g of trimethylamine solution (31–35 wt.% in ethanol, Aldrich) in 100 ml of Ethyl Acetate while stirring in an ice bath. The solution is allowed to stir overnight forming large crystals of C_4tMABr (50% yield based on 1-bromobutane). The solution is then filtered and dried in a dessicator containing zeolite NaX (Aldrich). The crystalline C_4tMABr is then ion exchanged to the hydroxide form following the procedure above.

Hexyltrimethylammonium hydroxide (C_6tMAOH) is synthesized by adding 1-bromohexane (Aldrich) to trimethylamine/ ethanol solution in a 1:2 molar ratio. The solution forms a viscous gel after stirring overnight. Excess

Table 1
Organic Structure Directing Agents used in this report

Cation structure	Name	Code	Solution appearance after CAC
	Tetramethylammonium	TMA^+	Homogeneous
	Butyltrimethylammonium	C_4tMA^+	Homogeneous
	Hexyltrimethylammonium	C_6tMA^+	Homogeneous/heterogeneous
	Heptyltrimethylammonium	C_7tMA^+	Homogeneous/heterogeneous
	Octyltrimethylammonium	C_8tMA^+	Heterogeneous
	Decyltrimethylammonium	$C_{10}tMA^+$	Heterogeneous
	Dodecyltrimethylammonium	$C_{12}tMA^+$	Heterogeneous

Preparation of homogeneous “clear” silicate solutions.

trimethylamine and ethanol are removed in a rotovap. The remaining white solid is washed with 200 ml cold ethyl acetate (Aldrich). The solid is recrystallized in an ethyl acetate/ethanol mixture overnight and the final solid is stored in a dessicator over zeolite NaX to dry. The final yield is 62% for the 1-bromohexane added. Heptyltrimethylammonium bromide (C_7tMABr) is synthesized following the same procedure with 1-bromoheptane (Aldrich). Both bromide forms are ion exchanged to the OH^- form following the above procedure.

For small-angle neutron scattering (SANS) measurements, the bromide forms of the SDAs are converted to the deuterated hydroxide forms (TMAOD, C_4tMAOD , C_6tMAOD , and C_7tMAOD). These are synthesized by mixing R^+Br^- (TMABr, from Aldrich and used as received) with deuterated water and silver oxide (Aldrich) in a 1.5:1 molar excess of silver oxide and stirring for 3–5 days.

Solutions prepared for conductivity and pH measurements are synthesized in a two step process. First, the SDA (TMAOH, (40 wt.%, Alfa Aesar), 0.101 M C_4tMAOH , 0.124 M C_6tMAOH , 0.125 M C_7tMAOH , 0.056 M C_8tMAOH , 0.128 M $C_{10}tMAOH$, 0.0823 M $C_{12}tMAOH$) is diluted with water to the desired concentration. Tetraethylorthosilicate (TEOS) is then added to these solutions to yield final molar ratios of $9 R^+OH^-:9500 H_2O:x SiO_2:4x EtOH$ where x varies from 2 to 40. These solutions are stirred for a minimum of 12 h, after which small-angle X-ray scattering (SAXS) patterns and conductivity are measured. SANS solutions are prepared in D_2O at a molar ratio of $9 R^+OD^-:9500 D_2O:40 SiO_2:160 EtOD$. Solids formed in solutions of C_8tMAOH , $C_{10}tMAOH$ and $C_{12}tMAOH$ after CAC are filtered washing with deionized water and dried in air prior to thermogravimetric (TGA) and X-ray diffraction (XRD) analysis.

Solutions to study the effect of ethanol are prepared at a molar ratio of $22 R^+OH^-:9500 H_2O:y SiO_2:(4333 + 4y) EtOH$ with y varying from 5 to 28 yielding solutions with similar total silica concentrations (mol/l) similar to those in the pure aqueous solutions. R^+OH^- , H_2O and excess EtOH are stirred for 30 min followed by the addition of TEOS. The solutions are then stirred overnight.

MCM-41 is prepared from sodium silicate solution (27 wt.% SiO_2 , Aldrich) at a molar ratio of 1 $C_{16}tMABr$: 1.89 SiO_2 :0.738 Na_2O :0.39 H_2SO_4 :160 H_2O . Water and $C_{16}tMABr$ (Aldrich) are added to the sodium silicate solution and stirred for 1 min followed by the addition of 1 M H_2SO_4 (Aldrich). The final solution is stirred for 30 min and then heated to 100 °C in a teflon lined autoclave for 4 days titrating the samples pH to 10 with 1 M H_2SO_4 each day.

2.2. Analytical methods

The determination of CAC curves is performed with a VWR Model 2052 EC Meter, and a Corning 355 pH/ion

analyzer using a SenTix high performance electrode. The pH meter is calibrated with standardized pH 10 and 12 buffer solutions (Alfa Aesar). The conductivity meter is calibrated using KCl standards at three different values (111, 12.8, 1.40 mS/cm).

SANS measurements are conducted on the 30 m instrument (NG3) at the National Institute of Standards and Technology at Gaithersburg, MD. The samples are placed in quartz cells of 4-mm pathlength. A constant neutron wavelength of 6 Å is used with a 1.2 m sample-to-detector distance. Software provided by NIST [21] is used for the normalization of the data and the subtraction of the sample holder scattering. SAXS experiments are conducted on a SAXSess camera SAXS system (Anton-Parr). Samples are placed in a vacuum-tight 1-mm diameter quartz capillary holder, and measured at 25 °C. $CuK\alpha$ radiation ($\lambda = 1.54$ Å) is used with a 265-mm sample-to-detector distance. The scattering patterns are collected on a phosphor imaging plate in the q -range 0.07 – 7.7 nm^{-1} . The darkcount rate is subtracted followed by the normalization of the pattern to the height of the primary beam signal. Desmearing is conducted by subtracting the signal from a normalized SDA/ H_2O sample. SAXS and SANS patterns are further analyzed using the Generalized Indirect Fourier Transform (GIFT) version 5-2000 software [22]. The subtracted scattering patterns are fitted with a form factor followed by indirect Fourier transform to obtain pair distance distribution functions (PDDFs).

TGA is performed on a TGA Q500 (TA instruments). The temperature for TGA measurements is ramped from room temperature to 800 °C at 10 °C/min in air.

XRD measurements are performed on a Phillips X'Pert X-ray diffractometer ($CuK\alpha$ radiation). The scattered intensity is measured in reflection mode over a 2θ range from 0.5 to 10 °C with a stepsize of 0.015 °C and 3 s per step. Patterns are normalized to the 100 peak maximum for comparison.

3. Results and discussion

The phase behavior of silica in aqueous solutions is studied in the presence of a family of quarternary ammonium cations with increasing chain length and hydrophobicity. Table 1 groups the cations based on the solution “appearance” after the addition of TEOS above the solutions critical point. First, the behavior of solutions forming homogeneous (transparent) solutions (TMA^+ and C_4tMA^+), will be compared to the SDAs used in the formation of M41S materials (C_8tMA^+ , $C_{10}tMA^+$ and $C_{12}tMA^+$) that form phase separated (heterogeneous) solutions. Next, SDAs having characteristics of both the homogeneous and heterogeneous mixtures (C_6tMA^+ and C_7tMA^+) are studied to determine the link between the phase separated and homogeneous solutions. Finally, the properties of a mixed solvent system with TMA^+ and $C_{10}tMA^+$ will be studied to determine the effect of hydrophobic forces on the silica phases formed.

3.1. Silica phase behavior in the presence of C_8 and larger cations

Beck et al. [10] showed that a family of mesoporous materials (M41S) with varying unit cell dimensions could be formed with quarternary ammonium surfactants by increasing the chain length of one of the alkyl chains. The chain lengths studied ranged from octyltrimethylammonium bromide ($((CH_3)_3NC_8H_{17}, C_8tMA^+)$) to cetyltrimethylammonium ($((CH_3)_3NC_{16}H_{33}, C_{16}tMA^+)$). We have reinvestigated such solutions by following the conductivity as a function of total silica concentration (Fig. 2a) for compositions $9 R^+OH^-:9500 H_2O:x SiO_2:4x EtOH$, with $x = 2$ to 40 for C_8tMA^+ and $C_{10}tMA^+$. Qualitatively, the conductivity follows the same trends as TMA^+ solutions prepared at the same composition (Fig. 1). All curves have two linear regions: one below CAC with a rapid change of the conductivity and one above with a smaller change in conductivity. The CAC values are $C_{10}tMA^+ = 0.055$ mol/kg, $C_8tMA^+ = 0.055$ mol/kg, $TMA^+ = 0.052$ mol/kg with $[OH^-]_{initial} = 0.0526$ mol/kg yielding essentially the same results previously reported for other TAA^+ cations [16]. However unlike our previous studies [15,16], these solutions differ after CAC.

For TMA^+ , the solutions after CAC are transparent. SAXS patterns of a TMA^+ sample after CAC (Fig. 2b) have a clear signal indicative of nanoparticles in solution (3–5 nm). Solutions with the same silica concentration prepared with C_8tMA^+ are opaque and exhibit a clear phase separation with a white precipitate forming after a few hours of stirring. No nanoparticle signal exists in the SAXS patterns of the C_8tMA^+ in the filtered supernatant above the white precipitate. The same behavior occurs for the $C_{10}tMA^+$ and $C_{12}tMA^+$ cations. The solutions of quarternary ammonium surfactants above C_8tMA^+ display two phases (Fig. 2c); before CAC silica forms monomers and small oligomers and after the CAC silica forms a silica/SDA precipitate phase.

The isolated silica precipitate is analyzed using XRD (Fig. 3) and TGA (Fig. 4). The XRD patterns of C_8tMAOH , $C_{10}tMAOH$ and $C_{12}tMAOH$ materials (Fig. 3a) display clear shifts in the first peak from $2.71^\circ 2\theta$ (d spacing = 32.6 \AA) for $C_{12}tMAOH$ to $3.50^\circ 2\theta$ (d spacing = 25.2 \AA) for C_8tMAOH . Comparison of the $C_{12}tMAOH$ sample to a hydrothermally prepared MCM-41 mesoporous material (Fig. 3b) using CTAB shows that the materials have similar structures. Both samples display three diffraction peaks with MCM-41 having peaks

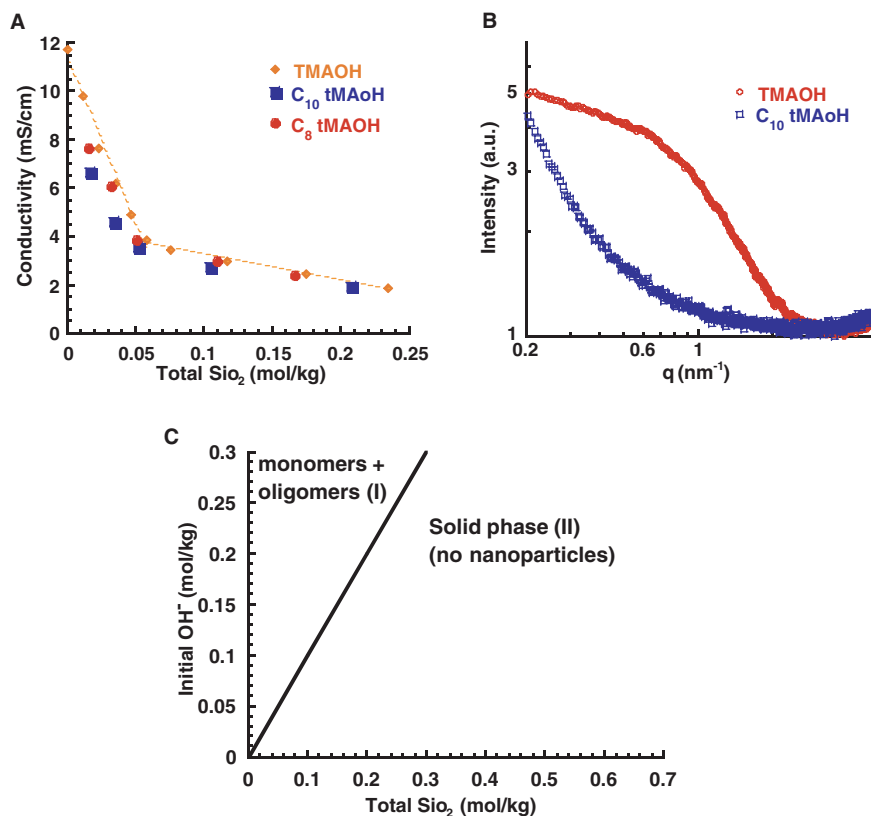


Fig. 2. (A) Conductivity vs. silica concentration for three organic cations. A $9 R^+OH^-:9500 H_2O:x SiO_2:4x EtOH$ molar ratio solution with $x = 2$ to 40 is measured for TMAOH, C_8tMAOH and $C_{10}tMAOH$. All three solutions display the same critical point. Dotted line represents fitted linear slopes for the two regions for TMAOH. (B) SAXS patterns (Intensity vs. scattering vector) of solutions measured at $x = 40$. The TMAOH solution shows a pattern characteristic of nanoparticles, but the C_8tMAOH solution is featureless in the region of interest (0.5 to 5 nm^{-1}). (C) Phase behavior of C_8 and larger cations. Two regions are present: a homogeneous solution of monomers and oligomers of silica, and a two phase region containing a white silica precipitate in equilibrium with the liquid phase.

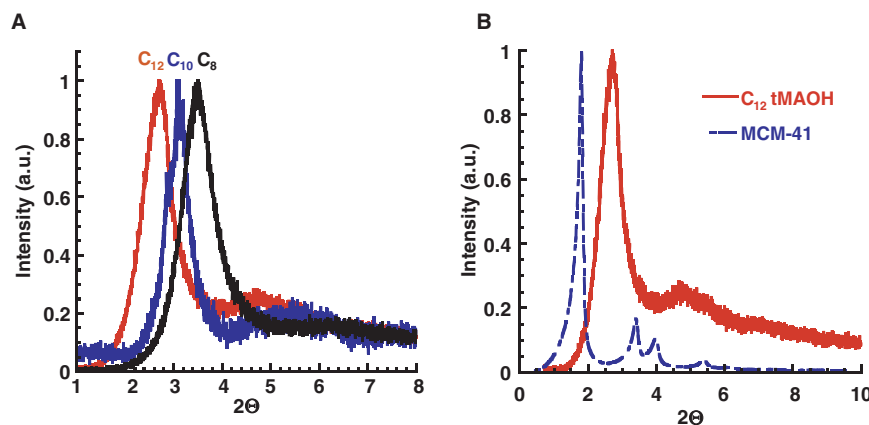


Fig. 3. XRD patterns of room temperature materials prepared with M41S cations. (A) Intensity versus the scattering angle is shown for C_8 tMAOH, C_{10} tMAOH, and C_{12} tMAOH. Peaks shift to larger d-spacings as the cation chain length increases. (B) Comparison of the room temperature mesoporous silicate and MCM-41 prepared at 100 °C. Both structures are hexagonal.

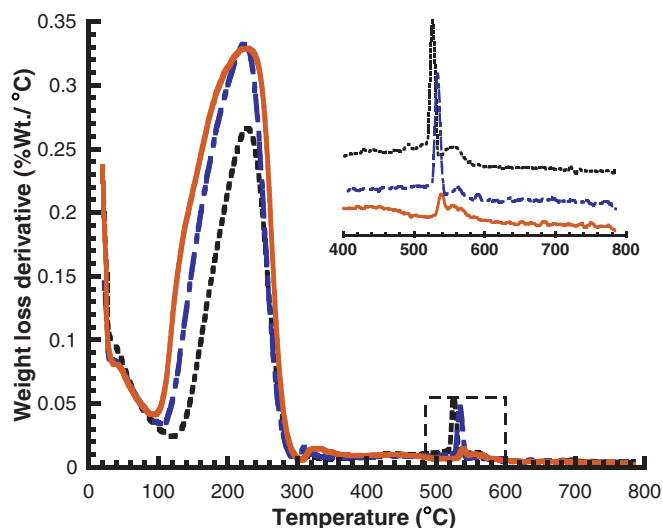


Fig. 4. First Derivative of weight loss traces during TGA analysis. At approximately 230 °C, the SDAs decompose; while at 550 °C, residual carbon deposits combust. The weight lost in the first peak is 2.00 g for C_{12} tMAOH, 1.40 g for C_{10} tMAOH and 1.22 g for C_8 tMAOH. The molar ratio of $R^+:\text{SiO}_2$ in the second peak is $\sim 1:90$ for all of the materials tested: C_{12} tMA Red (—), C_{10} tMA, Blue (---), C_8 tMA, Black (- - -).

characteristic of a sample made with a longer chain SDA. Indexing the XRD pattern of the C_{12} tMAOH product is consistent with hexagonal ordering ($d_{110} = 18.7$ Å and $d_{200} = 16.0$ Å). This is all consistent with the report by Beck et al. [10] who showed that increasing the surfactant chain length led to products with increasing pore size. XRD measurements ranging from 5 to 50 °C 2θ were also performed (Supplemental Figure) and showed only one broad peak indicative of amorphous silica.

TGA traces (Fig. 4) of the solid sample contain two peaks representative of the SDA decomposition and desorption, also present in the M41S materials [10]. The first peak represents SDA decomposition and silica condensation. This peak has a maximum at the same location

as neat decyltrimethylammonium bromide (C_{10} tMABr). The small second peak at ~ 530 °C (image enlarged in inset) may be caused by occluded SDA within the silica.

There are some differences between the materials reported here and the M41S series. First, the XRD peaks are broadened significantly and the 110 and 200 reflections are nearly indistinguishable for C_{10} tMAOH and C_8 tMAOH samples. Also, a second peak in the TGA analysis of M41S materials is not observed for the room temperature prepared materials reported here. Gross et al. [23], using eicosyltrimethylammonium solutions, showed that hydrothermal treatment will lead to changes in the internal silica connectivity of the material and sharpening of the XRD patterns. This condensation leads to a more ordered structure with less internal silanol groups. M41S materials prepared by Beck et al. [10] were heated to 150 °C for 48 h, whereas our solids are extracted from room temperature precursor solutions. The more extensive condensation of silica for the M41S materials may explain the difference in the peak broadening between the reported materials and the M41S series. In general though, the room temperature materials do exhibit the same structural properties as M41S materials: both have hexagonal structures and occluded internal SDA.

A link between nanoparticles and mesoporous materials, therefore, is observed after crossing CAC. However to gain some insight into the mechanism of mesoporous formation, we next study the transition SDA region (Table 1) for C_6 – C_8 tMA.

3.2. Silica phase behavior in the presence of mid-sized cations

Conductivity (Fig. 5a) of solutions containing mid-sized cations (C_4 tMAOH, C_6 tMAOH and C_7 tMAOH) also exhibit a critical point at a 1:1 $\text{SiO}_2:[\text{OH}^-]_{\text{initial}}$ molar ratio. Unlike the C_8+ cations, SAXS patterns (Fig. 5b) of the solutions from the region following CAC contain

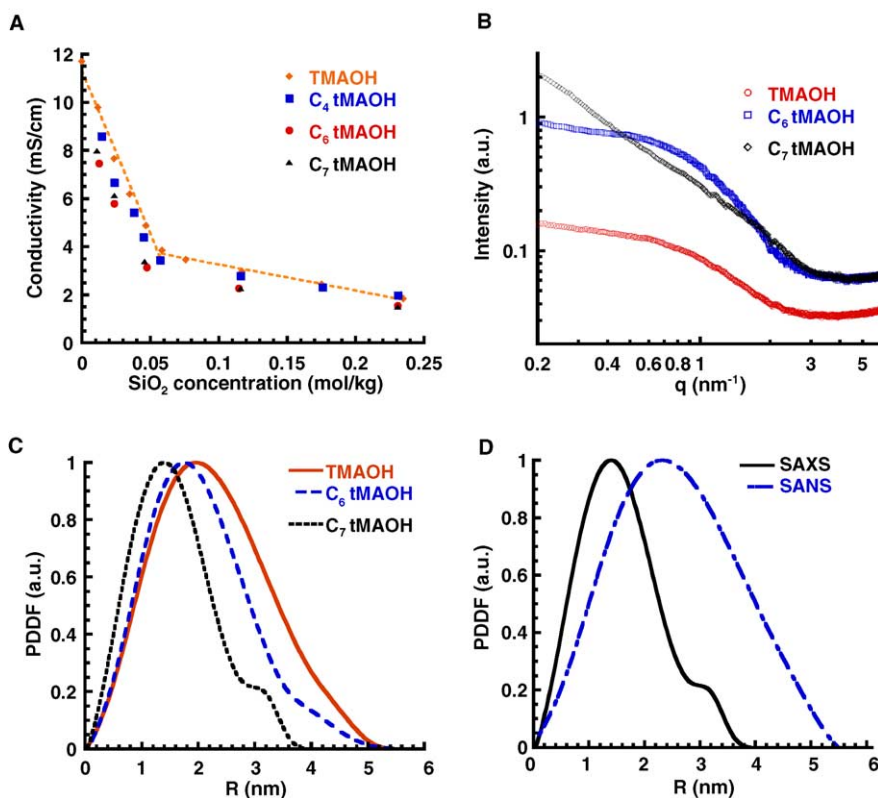


Fig. 5. C₄–C₇tMA cations CAC and particle size. (A) Variation of conductivity with increasing silica concentration for TMAOH, C₄tMAOH, C₆tMAOH, and C₇tMAOH at a molar ratio of 9 R⁺OH⁻:9500 H₂O:x TEOS:4x EtOH where x varies from 2 to 40. As with the M41S materials, a CAC is observed at approximately a 1:1 molar ratio of SiO₂:[OH⁻]_{initial}. Dotted lines represent fitted linear slopes for the two regions for TMAOH. (B) SAXS patterns of TMAOH, C₆tMAOH and C₇tMAOH at $x = 40$. TMAOH and C₆tMAOH have scattered intensity trends consistent with the formation of uniform nanoparticles. The C₇tMAOH pattern displays a nanoparticle peak at higher q than the other SDAs and has residual scattering consistent with large particles outside of the measurement range. (C) X-ray PDDFs of TMAOH, C₆tMAOH and C₇tMAOH at $x = 40$. The nanoparticle size appears to decrease with increasing cation chain length. (D) SAXS/SANS PDDF comparison for C₇tMAOH at $x = 40$. The difference between the PDDFs are characteristic of a core-shell particle with a variation between core and shell scattering length densities. PDDF fitted from $q = 0.9\text{--}5\text{ nm}^{-1}$ for the C₇tMA⁺ nanoparticle.

nanoparticles similar to the ones observed with symmetric TAA⁺ species [15]. The solution, though, is not transparent as with symmetric TAA⁺ cations. These solutions are translucent, and in the case of C₇tMAOH, a small quantity of white precipitate is visible in the solution after CAC. The SAXS pattern for C₇tMAOH illustrates this behavior as the pattern has a weak signal attributed to nanoparticles. However, this signal does not level off at low q as would be predicted for uniform nanoparticles. This additional scattering intensity may represent a second particle population not seen in C₆tMAOH and TMAOH patterns measured at the same composition. The presence of larger particles is clear from the solution appearance but their characterization is beyond the scope of this paper.

The nanoparticle core size and shape is uniform for the mid-sized cations. The SAXS patterns of C₆tMAOH and TMAOH, Fig. 5b, are nearly identical except for increase in the overall particle scattering and background. The scattering of extremely large particles could cause the overall scattering intensity to increase without a signal observed in the final SAXS pattern. C₇tMAOH solutions contain nanoparticles with smaller core sizes as based on a pair dis-

tance distribution function (PDDF) peak maximum (40 Å, Fig. 5c) compared to TMAOH (56 Å) and C₆tMAOH (50 Å). The nanoparticles still retain the core-shell structure present for TAA⁺ nanoparticles. The comparison of SAXS and SANS results for C₇tMAOH, Fig. 5d, shows a clear difference in the nanoparticle size, which arises from the difference in scattering length densities, ($\Delta\rho = \rho_{\text{SDA}} - \rho_{\text{solvent}}$), between the SDA and different solvents. For SAXS, $\Delta\rho$ for C₇tMA⁺ and H₂O is $1.64 \times 10^{-6}\text{ Å}^{-2}$; while for SANS in D₂O, $\Delta\rho$ is $6.75 \times 10^{-6}\text{ Å}^{-2}$. Scattered signal intensity is proportional to $\Delta\rho$ [2] resulting in an order of magnitude difference in the final scattered intensities from the particle shell in SAXS and SANS [24].

Preliminary analyses of the SANS patterns for the C₇tMAOH nanoparticle requires the inclusion of interparticle forces which are simulated in this case with a Hayter–Penfold [25] interparticle force model. SANS pattern analysis [26] shows that the best-fit particle morphology for the C₇tMAOH nanoparticle is a core-shell prolate ellipsoid. The particle core has long and short radii of 19 Å and 12 Å. The simulated shell is *not* uniform with a thickness of 14 Å at the narrow ends of the prolate ellipse and a thick-

ness of 4 Å in the center. Analysis of core-shell cylinder models also led to particles with similar final dimensions.

The experimental results, from the C₈–C₁₂ and C₆–C₇ cations when combined with previous experiments on the TAA⁺ system, show a fundamental connection between the synthesis of microporous and mesoporous materials. First, the phase behavior of silica in aqueous solutions is independent cation's potential to self-assemble. C₈tMA⁺, C₁₀tMA⁺, and C₁₂tMA⁺ are all capable of forming micelles at relatively low SDA concentrations. The CACs, however, for all three surfactants are indistinguishable (0.052–0.055 mol SiO₂/kg H₂O). For C₈tMA⁺ and C₁₀tMA⁺, the critical micelle concentrations (CMC) for organization (0.293 mol R⁺/kg H₂O for C₈tMA⁺ [27], 0.068 mol R⁺/kg H₂O for C₁₀tMA⁺ [28]) are above CAC. While for C₁₂tMA⁺, CMC (0.016 mol R⁺/kg H₂O) [28] is three times lower than CAC. Therefore, regardless of the presence of micelles in solution, the conductivity and CAC behavior of silica is identical. Second, the formation of nanoparticles occurs in all SDA solutions from TMA⁺ to C₇tMA⁺. These nanoparticles have similar sizes and core-shell structures. Furthermore, from XRD and TGA analysis, it is apparent that the formation of mesoporous materials does occur at room temperature after crossing CAC although the material contains more defects and is less ordered than the hydrothermally treated materials. The link between microporous and mesoporous materials, therefore, is through the nanoparticles present in the initial synthesis solutions. Nanoparticles and mesoporous materials are similar in nature as micelles are to liquid crystals.

Microporous materials, however, are not of a similar nature requiring heating to form.

This finding supports the current trend in the development of the mesoporous material formation mechanism away from the original liquid crystal templating (LCT) mechanism [29,30]. The LCT mechanism proposed that the onset of silica aggregation was related to the formation of surfactant micelles in solution [29]; however, we have shown that silica condensation is not related to the presence of micelles in solution. Similar conclusions were reached through fluorescence measurements of the counterions present on the surface of CTAB micelles [31–33]. These measurements showed that silica was not found to aggregate on the surface of the surfactant micelles as required for an LCT mechanism. We propose a different mechanism for mesoporous material formation presented in Fig. 6.

The aggregation of soluble silica into nanoparticles and mesoporous solids can be viewed within the thermodynamic framework of self-assembly [20,34]. The self-assembly of surfactants into micelles occurs when the chemical potential of the surfactant in solution is equal to the chemical potential of the surfactant in the micelle [20]. For the silica/water/SDA system prior to CAC (Phase I, Fig. 6), the chemical potential, μ_1 , is such that the silica monomer has a lower chemical potential than the silica nanoparticle ($\mu_1 < \mu_2$), similar to a surfactant molecule prior to CMC. Therefore, reaction 2 does not proceed to any measurable extent. At CAC, silica in the aqueous phase (Phase I) and in the nanoparticle (Phase II) have equal chemical

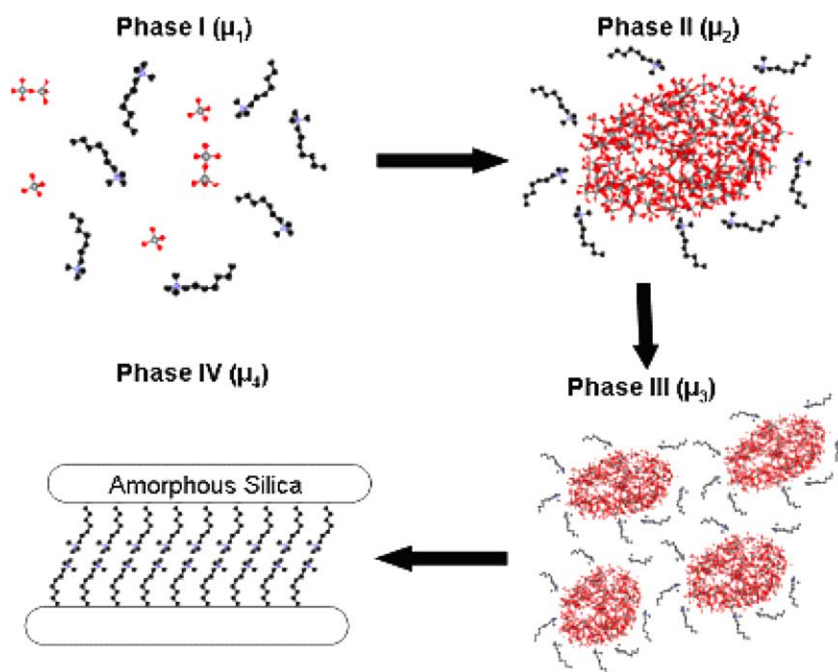


Fig. 6. Hypothetical phase transformation process for silica solutions of C₈tMA⁺ and larger. The formation of mesoporous materials can be thought of as proceeding through a series of phases of increasingly lower chemical potential. For all cations, monomeric silica solutions (Phase I) proceed to form nanoparticles (Phase II) after the solution CAC. In solutions with strongly hydrophobic SDAs, these nanoparticles solutions aggregate to form a solid phase (Phase III). The phase can reorganize into an extended periodic structure (Phase IV) with the lowest chemical potential.

potentials, ($\mu_1 = \mu_2$) leading to self-assembly. For cation chain lengths below C_6tMA^+ , the nanoparticle phase is the most stable silica phase at room temperature. However for C_8tMAOH and beyond, the solid precipitate is the most stable state.

The question arises as to what causes the formation of two different lowest energy states in the silica/water/SDA system. The answer lies in the forces governing the stability of nanoparticle sols with SDAs of different chain lengths. As described above the stability of the nanoparticle is governed by three components: the condensation of silica, the formation of the electrical double layer and surface forces. For the nanoparticle, electrostatic repulsive forces probably dominate the solution behavior. However, for chain lengths above C_6tMA^+ , the electrostatic forces are superseded by the attractive hydrophobic forces between the SDA in the double-layer of the nanoparticles. These attractive forces drive the particles toward aggregation (similar to the formation of liquid crystals from micelles) [34]. Even though these solutions are in many cases below the critical micelle concentration of the SDA, the increase in the local concentration of the SDA on the nanoparticle surfaces, leads to the collapse of the stable nanoparticle suspension. The solid that is formed in Phase III is the result of this collapse and eventually reorganizes into a lower chemical potential extended structure (Phase IV, μ_4). In the final state, μ_4 is equal to μ_1 because silica is in equilibrium in the two phases.

This hypothesis is in line with the conclusions reached by Vartuli et al. [14], who connected variations in the liquid crystal structure with changes in the SDA:SiO₂ molar ratio for CTAOH. Their experiments also show that the dominant transition occurs at CAC of the solutions. Stable mesoporous materials were formed at concentrations near or above CAC where the silica solution will have proceeded to Phase IV. For large surfactants, Phase II and Phase III are hypothetical (not observed experimentally) but are helpful to visualize the formation of mesoporous materials.

It was also observed [14] that the silica concentration was critical in determining the mesoporous phase present with lower silica concentrations leading to the cubic MCM-48 and higher concentrations forming hexagonal MCM-41. Regular solution theory [35] predicts that the solid should have a higher concentration of the least soluble component. In this case, CTA^+ is the least soluble component and would be the dominant solid component at concentrations below or near CAC leading to the formation of cubic MCM-48. Increasing the silica concentration causes an increase in the SiO₂:R⁺ molar ratio in the solid phase until a composition is reached leading to a transition from the cubic to hexagonal structure.

3.3. Controlling particle aggregation in mixed solvents

The role of hydrophobic forces in the formation of extended structures could be tested by preparing nanoparticles in the presence of ethanol, because by adding ethanol to the solutions, the hydrophobic interactions leading to the aggregation of nanoparticles are reduced. As in the aqueous solutions, the solution conductivity was followed as a function of increasing silica concentration (Fig. 7a) for TMA⁺ and C₁₀tMA⁺ (22 R⁺OH⁻:9500 H₂O:y SiO₂: (4333 + 4y) EtOH with y varying from 5 to 28). The behavior is different. There is no clear CAC in the ethanolic solution. Recall that in alcohol solutions, silica has been shown [36] to be essentially insoluble. This behavior is apparent in the conductivity measurements with the curves displaying no drastic change in the slope before or after CAC. In these solutions, Phase I is not detectable and silica is forced to self-assemble immediately.

SAXS patterns of the solutions display weak nanoparticle scattering intensities at silica concentrations as low as 0.013 mol/kg or 1/5 the aqueous solution CAC. Nanoparticle sizes are smaller than those present in aqueous solutions, but are similar for both the TMA⁺ and C₁₀tMA⁺ solutions. Both solutions are homogeneous with no pre-

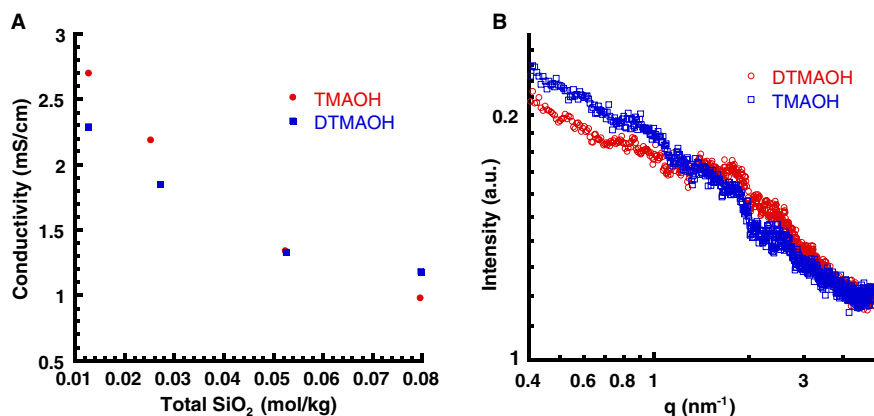


Fig. 7. Silica phase behavior in the presence of mixed solvents. (A) Conductivity with varying silica concentrations indicates the absence of a CAC for both TMA⁺ and C₁₀tMA⁺. (B) SAXS patterns of the mixed solvent solutions display nanoparticle signals which are similar for both C₁₀tMAOH and TMAOH. The final solutions are both transparent and uniform.

precipitate forming in the $C_{10}tMA^+$ solutions, but are very sensitive to silica concentration with gels forming at significantly lower concentrations than observed in aqueous solutions. These results show that hydrophobic forces are important in the destabilization of nanoparticle solutions required to form mesoporous materials.

4. Conclusions

The phase behavior of aqueous silica has been studied in the presence of a family of structure directing agents that lead to the formation of M41S materials and compared to our recent work on tetraalkylammonium cations (TAA^+). For both cation types, the solution displays the same critical behavior with a critical aggregation concentration occurring at a 1:1 molar ratio of $SiO_2:[OH^-]_{initial}$. The phases present are different with M41S SDAs leading to a white precipitate with no nanoparticles in the final solution in contrast to the stable nanoparticle suspensions formed in tetraalkylammonium solutions. SDAs in the transition regime between TAA^+ and M41S also display the same silica critical behavior, but yield “hybrid” solutions that contain both nanoparticles as well as the solid. The driving force for both microporous and mesoporous materials is the onset of silica aggregation that can lead to stable nanoparticle suspensions or phase separated solutions depending on the hydrophobic forces impacting the SDA. Measurements on mixed solvent systems containing ethanol and water verify the importance of hydrophobic forces with stable nanoparticle suspensions forming for $C_8-C_{12}tMA^+$ and for TMA^+ and C_4tMA^+ SDAs.

Acknowledgments

This work was funded by the National Science Foundation under Grant No. 0103010. We acknowledge Jeff Rimer for his assistance in gathering the SANS data and Kaveri Sawant for the preparation of MCM-41. Thermogravimetric analysis measurements were performed in the Center for Composite Materials at the University of Delaware. This work utilized facilities supported in part by the National Science Foundation under Agreement No. DMR-9986442 and DMR-0404153. We acknowledge the support of the National Institute of Standards and Technology, US Department of Commerce, in providing the neutron research facilities used in this work.

Appendix A. Supplementary data

Supplementary data associated with this article can be found, in the online version, at [doi:10.1016/j.micromeso.2005.10.048](https://doi.org/10.1016/j.micromeso.2005.10.048).

References

- [1] O. Ikkala, G. ten Brinke, *Chem. Comm.* (2004) 2131–2137.
- [2] A.A. Tseng, A. Notargiacomo, *J. Nanosci. Nanotech.* 5 (2005) 683–702.
- [3] M.E. Davis, *Nature* 417 (2002) 813–821.
- [4] M.E. Davis, *Science* 300 (2003) 438–439.
- [5] C.S. Cundy, P.A. Cox, *Chem. Rev.* 103 (2003) 663–701.
- [6] C. Sanchez, G. Soler-Illia, F. Ribot, D. Grosso, *Comp. Rend. Chim.* 6 (2003) 1131–1151.
- [7] F. Schuth, W. Schmidt, *Adv. Mater.* 14 (2002) 629–638.
- [8] A. Stein, *Adv. Mater.* 15 (2003) 763–775.
- [9] H. van Bekkum, E.M. Flanigan, P.A. Jacobs, J.C. Jansen (Eds.), *Introduction to Zeolite Science and Practice*, Elsevier, New York, 2001.
- [10] J.S. Beck, J.C. Vartuli, W.J. Roth, M.E. Leonowicz, C.T. Kresge, K.D. Schmitt, C.T.W. Chu, D.H. Olson, E.W. Sheppard, S.B. McCullen, J.B. Higgins, J.L. Schlenker, *JACS* 114 (1992) 10834–10843.
- [11] D.Y. Zhao, Q.S. Huo, J.L. Feng, B.F. Chmelka, G.D. Stucky, *JACS* 120 (1998) 6024–6036.
- [12] Q.S. Huo, D.I. Margolese, G.D. Stucky, *Chem. Mater.* 8 (1996) 1147–1160.
- [13] J.S. Beck, J.C. Vartuli, G.J. Kennedy, C.T. Kresge, W.J. Roth, S.E. Schramm, *Chem. Mater.* 6 (1994) 1816–1821.
- [14] J.C. Vartuli, K.D. Schmitt, C.T. Kresge, W.J. Roth, M.E. Leonowicz, S.B. McCullen, S.D. Hellring, J.S. Beck, J.L. Schlenker, D.H. Olson, E.W. Sheppard, *Chem. Mater.* 6 (1994) 2317–2326.
- [15] J.M. Fedeyko, D.G. Vlachos, R.F. Lobo, *Langmuir* 21 (2005) 5197.
- [16] J.M. Fedeyko, J.D. Rimer, R.F. Lobo, D.G. Vlachos, *J. Phys. Chem. B* 108 (2004) 12271–12275.
- [17] G.W. Castellan, *Physical Chemistry*, The Benjamin/Cummings Publishing Company, Inc., 1983.
- [18] S.A. Greenberg, *JACS* 80 (1959) 6508–6511.
- [19] J.D. Rimer, D.G. Vlachos, R.F. Lobo, *Langmuir* 21 (2005) 8960–8971.
- [20] J. Israelachvili, *Intermolecular & Surface Forces*, New York, Academic Press, 1992.
- [21] S. Kline, NIST Center for Neutron Research, SANS Data Reduction Software, 2001.
- [22] O. Glatter, GIFT for Windows, 1999.
- [23] A.F. Gross, S. Yang, A. Navrotsky, S.H. Tolbert, *J. Phys. Chem. B* 107 (2003) 2709–2718.
- [24] L.A. Feigin, D.I. Svergun, *Structure Analysis by Small-Angle X-Ray and Neutron Scattering*, Plenum Press, 1987.
- [25] J.P. Hansen, J.B. Hayter, *Mol. Phys.* 46 (1982) 651–656.
- [26] S. Kline, NIST SANS fitting procedures for Igor Pro.
- [27] R. Zielinski, *J. Coll. Int. Sci.* 235 (2001) 201–209.
- [28] P. Debye, *J. Phys. Coll. Chem.* 53 (1949) 1–8.
- [29] J.C. Vartuli, C.T. Kresge, M.E. Leonowicz, A.S. Chu, S.B. McCullen, I.D. Johnsen, E.W. Sheppard, *Chem. Mater.* 6 (1994) 2070–2077.
- [30] C.-Y. Chen, S.L. Burkett, H.-X. Li, M.E. Davis, *Micro. Mater.* 2 (1993) 27–34.
- [31] R. Zana, J. Frasc, M. Soudard, B. Lebeau, J. Patarin, *Langmuir* 15 (1999) 2603–2606.
- [32] R. Zana, J. Frasc, M. Soudard, B. Lebeau, J. Patarin, *Abstr. Amer. Chem. Soc.* 218 (1999) U248.
- [33] J. Frasc, B. Lebeau, M. Soudard, J. Patarin, R. Zana, *Langmuir* 16 (2000) 9049–9057.
- [34] P.C. Hiemenz, R. Rajagopalan, *Principles of Colloid and Surface Chemistry*, Marcel Dekker, New York, 1997.
- [35] P.M. Holland, D.N. Rubingh, *J. Phys. Chem.* 87 (1983) 1984–1990.
- [36] R.K. Iler, *The Chemistry of Silica*, John Wiley, 1979.